# A Lagrangian Finite Element Treatment of Transient Gravitational Waves in Compressible Viscous Fluids

## Ryszard Staroszczyk

Institute of Hydro-Engineering of the Polish Academy of Sciences,
Kościerska 7, 80-328 Gdańsk, Poland, e-mail: rstar@ibwpan.gda.pl

**Abstract.** In this paper the problem of transient gravitational wave propagation in a viscous compressible fluid is investigated. The problem is formulated in the Lagrangian description and is solved numerically by a finite element method. In computations either fixed in space or moving meshes that follow the material fluid particles are used with the purpose to compare their numerical performance. As illustrations, results of numerical simulations carried out for plane flows in a domain of simple geometry are presented. First, the finite element results are compared with available experimental data for the case of small-amplitude waves in order to validate the numerical model. Then, the problem of large-amplitude transient water wave propagation over a horizontal bottom, involving the wave reflection at a rigid wall, is considered. For the flow parameters typical of a laboratory flume, the evolution of the free-surface elevation and the time variations of the surface displacements at chosen locations are shown for a range of different moving wall amplitudes and excitation times.

## Notations

| | | |
|---|---|---|
| $\boldsymbol{b}$ | – | body force vector; |
| $c$ | – | speed of sound; |
| $d^*$ | – | wave-maker horizontal displacement amplitude; |
| $\boldsymbol{D}$ | – | strain-rate tensor; |
| $\boldsymbol{F}$ | – | referential deformation gradient tensor; |
| $\boldsymbol{G}$ | – | spatial deformation gradient tensor; |
| $g$ | – | acceleration due to gravity; |
| $H$ | – | still water depth; |
| $\boldsymbol{I}$ | – | unit tensor; |
| $J$ | – | deformation Jacobian; |
| $K$ | – | compressibility modulus; |
| $L$ | – | water flume length; |
| $\boldsymbol{L}$ | – | spatial velocity gradient; |

| $n, N$ | – | unit normal vector in spatial and referential coordinates; |
|---|---|---|
| $p$ | – | hydrostatic pressure; |
| $s, S$ | – | unit tangent vector in spatial and referential coordinates; |
| $t$ | – | time; |
| $t^*$ | – | characteristic time scale; |
| $v$ | – | fluid velocity vector; |
| $x, X$ | – | spatial and referential position vectors; |
| $\nabla^2$ | – | Laplacian operator; |
| $\Phi_j \ (j = 1, 2, 3)$ | – | interpolation functions; |
| $\kappa, \mu$ | – | fluid viscosities; |
| $\varrho, \varrho_0$ | – | current and referential fluid densities; |
| $\sigma$ | – | Cauchy stress tensor. |

## 1. Introduction

Numerical simulations of fluid flows are traditionally based on the Eulerian (or spatial) formulation of the governing equations. This approach has been successful in solving a large variety of problems in fluid mechanics, in particular the flow problems involving domains with fixed boundaries. The method has also been successful in dealing with certain problems in which part of the fluid domain boundary moves, and a classical example of such a problem is the gravitational water wave propagation phenomenon (Idelsohn et al 1999, Van Brummelen et al 2001). However, in problems in which the flow domain geometry changes rapidly in time, as, for instance, the shape of the liquid free surface or the shape of the liquid–engineering structure interface, and when complex non-linear phenomena occur, the Eulerian description encounters serious limitations and often turns out inadequate. The latter is largely due to difficulties associated with the sufficiently accurate tracing of the fluid domain moving boundaries, which is required for maintaining the stability of numerical schemes applied. For this reason, a natural way of solving fluid flow problems in which changing spatial domains occur is to apply the Lagrangian description, in which individual fluid particles are followed during an analysis. Compared to the spatial description, the Lagrange method has a potential of increased numerical stability due to the lack of convective terms appearing in the momentum equations in the Eulerian schemes. Additionally, the treatment of boundary conditions is much easier in the Lagrangian formulation, as they are imposed on material surfaces, that is the surfaces which do not move in fixed referential coordinates. With an idea to exploit the above advantages of the Lagrangian method, more and more attempts to employ this approach have been made over the past two decades, usually within the framework of the finite element method (Ramaswamy and Kawahara 1987, Radovitzky and Ortiz 1998, Feng and Perić 2000, Parrinello and Borino 2007). However, the numerical implementation of the Lagrangian approach encounters serious difficulties. These are due to very

large deformations and their rates that typically occur in liquid flows. Such large deformations are very hard to capture in any method in which a discrete mesh of a fixed (that is unchanged through computations) topology is used. Thus, to improve the numerical performance of the conventional Lagrangian method, one can modify it by either introducing a deformable mesh whose nodes move together with selected material particles, or by applying a technique of adaptive remeshing. This, however, usually gives rise to large distortions of the mesh (with highly degenerated cells) in the former case, or increases significantly computational costs in the latter case.

In order to overcome the afore-mentioned numerical problems occurring in the methods based on the Lagrangian description, a number of new promising variants of the method have been recently developed. Among them is the Arbitrary Lagrangian-Eulerian (ALE) method used by Braess and Wriggers (2000), Souli and Zolesio (2001) and Rabier and Medale (2003), in which the numerical grid imposed on the fluid domain moves in some arbitrary (that is unphysical) way to ensure that the distortion of individual grid cells is minimized. In this way the numerical stability is improved, allowing longer time steps to be applied. A qualitatively distinct Lagrangian approach is that based on so-called Particle Methods, in which all the physical properties of the continuum are represented by a discrete collection of material particles that are followed during a computation. To this group of methods belong, in particular, the Finite Point Method (FPM) applied in fluid mechanics by Oñate et al (1996a, b), Löhner et al (2002) and Ortega et al (2007), and the Particle Finite Element Method (PFEM) employed by Idelsohn et al (2003, 2004), Aubry et al (2005) and Idelsohn et al (2006) to analyse incompressible viscous fluid flows. While the FPM represents a fully meshless approach, the PFEM is a mesh-based approach in which, in order to evaluate interaction forces between individual particles, a new mesh is generated at each time step to connect those particles.

Very recently, Del Pin et al (2007) have proposed a method in which the PFEM and the ALE approaches are combined in such a way that the first, particle method, is used to describe fluid particles on the free surface and the fluid–structure interface, while the latter, ALE method, is applied to the rest of the fluid domain, on which a moving grid is imposed. This hybrid method has enabled the solving of such numerically challenging problems as water sloshing in a tank, dam collapse, wave breaking on a beach due to shoaling, and falling of solid bodies into a water container.

In the present work, the Lagrangian formulation is used to analyse the transient problem of non-linear free-surface waves propagating in a viscous fluid by applying a mesh-based finite element method. The fluid is treated as a Newtonian, compressible, barotropic liquid, the properties of which are described by two viscosity parameters. The surface waves are assumed to be generated by the motion of one of rigid boundaries enclosing the fluid domain, on which the displacements are prescribed. Numerical simulations are conducted for plane flows in a finite domain

of simple geometry. Time integration of the ensuing semi-discrete system of equations is carried out by applying the weighted residual $\theta$-method, with the Picard iterative method used to ensure the solution convergence. For illustration purposes, an idealized case of the transient water wave propagation over a horizontal bed, with the liquid initially occupying a rectangular domain, is investigated. The initially still liquid is set in motion by moving a vertical rigid wall situated at one of the ends of the water domain. In the numerical method developed, two different mesh strategies are explored in order to examine their numerical performance. In the first approach, the discrete mesh, once generated for the initial material configuration, is kept fixed in space throughout the computations. In the second approach, the mesh is updated after each discrete time step, by attaching the discrete nodes to a set of selected fluid material particles, and moving these nodes accordingly as the particles change their spatial positions in time.

The outline of the paper is as follows. In Section 2 the governing equations, describing the behaviour of a general class of two-viscosity Newtonian compressible fluids, and formulated in the Eulerian description, are summarized. These equations are subsequently transformed into the Lagrangian forms in Section 3. The following Section 4 is devoted to the finite element formulation of the problem, including the spatial discretization and time integration methods. Then, in Section 5, a few numerical examples for the transient water wave propagation problem are presented, starting from a comparison between experimental data and FE results, and finally some conclusions are given in Section 6.

## 2. Problem Statement

Let introduce rectangular Cartesian coordinate system with origin $O$ and coordinate axes $x_i$ ($i = 1, 2, 3$), and let $t$ denote time. A fluid particle position at time $t$ relative to the chosen coordinate frame is defined by a vector $\boldsymbol{x}$ with components $x_i(t)$, and the current particle velocity is given by a vector $\boldsymbol{v}$ with components $v_j(x_i, t)$, ($i, j = 1, 2, 3$).

The law of mass conservation expressed in the adopted current (spatial, or Eulerian) reference frame $Ox_i$ is given by the continuity equation

$$\frac{\mathrm{D}\varrho}{\mathrm{D}t} + \varrho \operatorname{div} \boldsymbol{v} = 0, \tag{1}$$

where $\varrho$ is the fluid density, $\mathrm{D}/\mathrm{D}t$ denotes the material (convected) time derivative, and $\operatorname{div}$ denotes the spatial divergence operator.

Linear momentum conservation balance, in the presence of body forces, yields the Cauchy equation of motion

$$\varrho \frac{\mathrm{D}\boldsymbol{v}}{\mathrm{D}t} = \operatorname{div} \boldsymbol{\sigma} + \varrho \boldsymbol{b}, \tag{2}$$

in which $\boldsymbol{\sigma}$ is the Cauchy stress tensor and $\boldsymbol{b}$ denotes the body force vector.

The fluid under consideration is assumed to be isotropic, viscous and compressible. The present analysis is restricted to the class of Newtonian viscous fluids, the physical behaviour of which is described by the following constitutive law (Chadwick 1999):

$$\boldsymbol{\sigma} = \left[-p + \left(\kappa - \tfrac{2}{3}\mu\right)\operatorname{tr}\boldsymbol{D}\right]\boldsymbol{I} + 2\mu\boldsymbol{D}. \tag{3}$$

In the above relation, $p$ is the hydrostatic pressure, $\kappa$ and $\mu$ are, respectively, the bulk and shear viscosities, $\boldsymbol{I}$ is the unit tensor, tr denotes the trace of a tensor, and $\boldsymbol{D}$ denotes the strain-rate tensor. The latter is defined as a symmetric part of the spatial velocity gradient, $\boldsymbol{L}$, by means of

$$\boldsymbol{L} = \operatorname{grad}\boldsymbol{v}, \quad \boldsymbol{D} = \tfrac{1}{2}\left(\boldsymbol{L} + \boldsymbol{L}^T\right), \tag{4}$$

where the superscript $T$ denotes the tensor transpose, and grad stands for the spatial gradient operator. In components, equations (4) read

$$L_{ij} = \frac{\partial v_i}{\partial x_j}, \quad D_{ij} = \frac{1}{2}\left(\frac{\partial v_i}{\partial x_j} + \frac{\partial v_j}{\partial x_i}\right), \quad (i, j = 1, 2, 3). \tag{5}$$

Substitution of the stress expression (3) into the equation of motion (2) yields the Navier-Stokes equation in the form:

$$\varrho\frac{\mathrm{D}\boldsymbol{v}}{\mathrm{D}t} = -\operatorname{grad}p + \mu\nabla^2\boldsymbol{v} + \left(\kappa + \tfrac{1}{3}\mu\right)\operatorname{grad}\operatorname{div}\boldsymbol{v} + \varrho\boldsymbol{b}, \tag{6}$$

where $\nabla^2(\cdot) = \operatorname{div}\left[\operatorname{grad}(\cdot)^T\right]$ is the vector Laplacian operator in the spacial description.

In general, the pressure $p$ and the viscosities $\kappa$ and $\mu$ can depend on the fluid density and temperature, as well as on invariants of $\boldsymbol{D}$. In this work, however, only isothermal flows are considered; that is, the effects of temperature are neglected. Further, the fluid viscosities are supposed to be constant (independent on $\varrho$ and $\boldsymbol{D}$), and the fluid motion is assumed to be barotropic, in which case the pressure is entirely determined by the fluid density. The pressure dependence on the density is adopted in the form commonly employed in water flow problems, namely,

$$\frac{\mathrm{D}\varrho}{\mathrm{D}t} = \frac{1}{c^2}\frac{\mathrm{D}p}{\mathrm{D}t}, \tag{7}$$

with $c$ being the speed of sound. On substituting the latter relation into (1), the mass conservation equation becomes

$$\frac{\mathrm{D}p}{\mathrm{D}t} + K\operatorname{div}\boldsymbol{v} = 0, \tag{8}$$

where $K = \varrho c^2$ is the fluid compressibility modulus.

In order to complete the problem statement, initial and boundary conditions must be specified. It is supposed that the fluid motion starts at time $t = 0$, and

at $t \leq 0$ the fluid velocities are zero, $\boldsymbol{v} = 0$, and the stress in fluid is that of the hydrostatic pressure, $\boldsymbol{\sigma} = -p\boldsymbol{I}$. The boundary condition are adopted in the standard forms:

$$
\begin{aligned}
\boldsymbol{n} \cdot (\boldsymbol{\sigma n}) &= t_n & \text{and} \quad \boldsymbol{s} \cdot (\boldsymbol{\sigma n}) &= t_s & \text{on} \quad \Gamma_\sigma, \\
\boldsymbol{v} \cdot \boldsymbol{n} &= v_n & \text{and} \quad \boldsymbol{v} \cdot \boldsymbol{s} &= v_s & \text{on} \quad \Gamma_v,
\end{aligned} \tag{9}
$$

where $t_n$ and $t_s$ are prescribed traction vector components normal and tangential to the boundary $\Gamma_\sigma$, $v_n$ and $v_s$ are prescribed velocity components normal and tangential to the boundary $\Gamma_v$, and $\boldsymbol{n}$ and $\boldsymbol{s}$ denote unit vectors normal and tangential to the respective boundaries. In most common situations, the boundary $\Gamma_\sigma$ is identical to the fluid free surface on which the traction forces are due to the action of atmosphere, while $\Gamma_v$ defines all solid (usually treated as rigid and impermeable) boundaries on which the fluid velocity components are determined by kinematical conditions imposed on the fluid–solid system.

## 3. Lagrangian Description of the Problem

In conventional fluid mechanics approach, the system of the Navier-Stokes and continuity equations, (6) and either (1) or (8), with relevant boundary conditions specified in (9), is solved in the spatial coordinate frame $Ox_i$, describing thus the motion of a fluid in its current (deformed) configuration. In order to follow the motion of individual material particles of a fluid, a fixed in space reference frame is introduced, which defines the positions of material particles at a reference time $t = 0$. Hence, a fixed rectangular Cartesian coordinate frame with the origin $O$ is adopted. Let $\boldsymbol{X}$ denote the position vector, with components $X_i$ ($i = 1, 2, 3$), describing a fluid particle position relative to $O$ at the reference time; that is, $\boldsymbol{x} = \boldsymbol{X}$ at $t = 0$. As the flow proceeds, at a subsequent time $t > 0$ the particle moves to a new position $\boldsymbol{x} = \boldsymbol{x}(\boldsymbol{X}, t)$. The way the particle moves in relation to its neighbourhood, measured in the referential (material, or Lagrangian) coordinates $X_i$, is described by the deformation gradient tensor, $\boldsymbol{F}$, defined by

$$
\boldsymbol{F}(\boldsymbol{X}, t) = \operatorname{Grad} \boldsymbol{x}(\boldsymbol{X}, t), \quad F_{ij} = \frac{\partial x_i}{\partial X_j}, \quad (i, j = 1, 2, 3), \tag{10}
$$

where Grad denotes the referential (material) gradient operator. We also introduce an inverse tensor

$$
\boldsymbol{G}(\boldsymbol{x}, t) = \boldsymbol{F}^{-1}(\boldsymbol{x}, t) = \operatorname{grad} \boldsymbol{X}(\boldsymbol{x}, t), \quad G_{ij} = \frac{\partial X_i}{\partial x_j}, \tag{11}
$$

defining the spatial deformation gradient tensor. Necessarily, due to smoothness conditions imposed on the functions $\boldsymbol{x}(\boldsymbol{X}, t)$ and $\boldsymbol{X}(\boldsymbol{x}, t)$ (Chadwick 1999),

$$
J = \det \boldsymbol{F} = (\det \boldsymbol{G})^{-1} > 0, \tag{12}
$$

with $J = 1$ at the initial, undeformed configuration, in which $\boldsymbol{F} = \boldsymbol{G} = \boldsymbol{I}$.

In principle, all the equations set in the spatial coordinates $x_i$ in the previous section can be derived in the referential coordinates $X_i$ by using the mapping $\boldsymbol{x} = \boldsymbol{x}(\boldsymbol{X}, t)$ and the definitions (10) and (11). In particular, the gradient and divergence operators expressed in both coordinate systems are connected through the following identities (Chadwick 1999, Liu 2002):

$$\text{Grad } \phi = \boldsymbol{F}^T \text{grad } \phi, \qquad \text{Grad } \boldsymbol{a} = (\text{grad } \boldsymbol{a})\boldsymbol{F},$$

$$\text{Div } \boldsymbol{a} = J \text{ div } \left( J^{-1} \boldsymbol{F} \boldsymbol{a} \right), \qquad \text{Div } \boldsymbol{A} = J \text{ div } \left( J^{-1} \boldsymbol{F} \boldsymbol{A} \right), \tag{13}$$

where grad and div refer to the current, and Grad and Div to the reference configurations, respectively. In Eq. (13), $\phi$, $\boldsymbol{a}$ and $\boldsymbol{A}$ denote, in order, arbitrary scalar, vector and second-order tensor fields. Further, the unit normal and tangent vectors, $\boldsymbol{n}$ and $\boldsymbol{s}$, appearing in the boundary conditions (9) specified in the spatial description, are related to their respective referential counterparts $\boldsymbol{N}$ and $\boldsymbol{S}$ by the formulae

$$\boldsymbol{n} = \frac{\boldsymbol{G}^T \boldsymbol{N}}{\left| \boldsymbol{G}^T \boldsymbol{N} \right|}, \qquad \boldsymbol{s} = \frac{\boldsymbol{G}^T \boldsymbol{S}}{\left| \boldsymbol{G}^T \boldsymbol{S} \right|}. \tag{14}$$

The application of the above transformation relations is the most consistent method of transferring the spatial forms of the flow equations into the respective referential forms. However, proceeding it this way gives rise to equations of a complicated structure. For this reason, an alternative approach is pursued here, in which the Navier-Stokes and continuity equations are expressed in components, instead of in tensorial forms (6) and (8), and then all the spatial derivatives are transformed into the corresponding referential derivatives by applying the chain rule of partial differentiation (or, equivalently, by employing Eq. $(13)_1$), and making use of the definition (11). Accordingly, for any scalar quantity $\phi$, including a vector component, the required transformation formula is given by

$$\frac{\partial \phi}{\partial x_i} = \frac{\partial \phi}{\partial X_j} \frac{\partial X_j}{\partial x_i} = G_{ji} \frac{\partial \phi}{\partial X_j}, \quad (i, j = 1, 2, 3), \tag{15}$$

where the summation convention for a repeated subscript is adopted.

Material time derivatives $D/Dt$ in the spatial description become the partial time derivatives $\partial/\partial t$ at fixed $\boldsymbol{X}$ in the referential description. Hence, on using the relations (15) in (6) and (8), the Navier-Stokes equation expressed in components becomes

$$J^{-1} \varrho_0 \frac{\partial v_i}{\partial t} = -G_{ji} \frac{\partial p}{\partial X_j} + \mu \, G_{jm} G_{km} \frac{\partial^2 v_i}{\partial X_j \, \partial X_k} +$$

$$+ \left( \kappa + \tfrac{1}{3}\mu \right) G_{jm} G_{ki} \frac{\partial^2 v_m}{\partial X_j \, \partial X_k} + J^{-1} \varrho_0 b_i, \tag{16}$$

and the continuity equation takes the form

$$K^{-1}J\frac{\partial p}{\partial t} + G_{jk}\frac{\partial v_k}{\partial X_j} = 0, \tag{17}$$

where it has been assumed that the compressibility modulus $K$ is independent of the fluid density. In derivation of the above two expressions, use has been made of the identity

$$J = \frac{\varrho_0}{\varrho}, \tag{18}$$

with $\varrho_0$ denoting the fluid density in the referential configuration. Obviously, $J \equiv 1$ in the case of an incompressible fluid. The equations (16) and (17) are supplemented by the boundary conditions expressed in the referential coordinates $X_i$ in terms of the unit vectors $N$ and $S$, replacing the vectors $n$ and $s$ in the conditions (9).

The relations (16) and (17) express the momentum and mass balances in terms of the current components of the deformation tensor $G$, the inverse of $F$. In view of the definition (10), since in the referential description the gradient and the time derivative commute, the following relation holds

$$\frac{\partial F_{ij}}{\partial t} = \frac{\partial}{\partial t}\left(\frac{\partial x_i}{\partial X_j}\right) = \frac{\partial \dot{x}_i}{\partial X_j} = \frac{\partial v_i}{\partial X_j}, \tag{19}$$

where the superimposed dot denotes the time derivative. The latter equation describes the evolution of $F$, and hence of $G$, in terms of the referential velocity gradient Grad $v$, and is used here to calculate, by time integration, the changes in the deformation gradient components as the deformation (flow) proceeds, starting from the initial configuration in which $F = G = I$.

The set of partial differential equations (16) and (17), complemented by boundary conditions defined in the referential coordinates, describes the flow problem in terms of the pressure $p$ and the velocity components $v_i$ ($i = 1, 2, 3$). This set of equations is solved numerically by applying a finite element method.

## 4. Finite Element Formulation

The present analysis is restricted to two-dimensional flows. Hence, plane spatial and referential rectangular coordinate systems $Ox_1x_2$ and $OX_1X_2$ are adopted, in which the axes $x_1$ and $X_1$ are directed horizontally, and the vertical axes $x_2$ and $X_2$ are directed upwards, see Figure 1. Accordingly, all the subscripts ($i, j, k$ and $m$) in the problem equations take the values 1 and 2. It is assumed that the only body force acting in the system is that due to gravity, so the vector $b$ has the components $b_1 = 0$ and $b_2 = -g$, with $g$ being the gravitational acceleration. The stress state in the fluid is measured here relative to the atmospheric pressure (treated as constant), and it is assumed that there are no forces acting tangentially to the free surface. Therefore, the fluid free surface boundary $\Gamma_\sigma$ is treated as traction-free; that is, both $t_n$ and
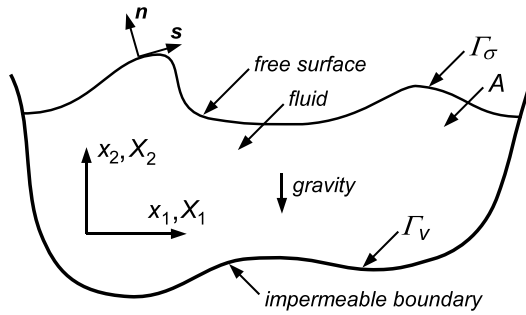
**Fig. 1.** Plane free-surface fluid flow problem definition

$t_s$ are zero in (9). The solid boundary $\Gamma_v$ enclosing the fluid domain is assumed rigid and impermeable. Hence, the velocity component $v_n$, normal to the boundary, is either zero on motionless parts of $\Gamma_v$, or is a prescribed time-dependent quantity on moving parts of $\Gamma_v$. Slip conditions are assumed along the whole boundary $\Gamma_v$, therefore no constraints are imposed there on the tangential velocity component $v_s$.

In the plane flow case, the components of the deformation gradient tensors $\boldsymbol{F}$ and $\boldsymbol{G} = \boldsymbol{F}^{-1}$ are related by

$$\boldsymbol{G} = J^{-1} \begin{pmatrix} F_{22} & -F_{12} \\ -F_{21} & F_{11} \end{pmatrix}, \quad J = \det \boldsymbol{F} = F_{11}F_{22} - F_{12}F_{21}. \tag{20}$$

The finite element solution of three differential equations (16) and (17) for $p$, $v_1$ and $v_2$ is based on a weak formulation of the latter equations, and the method of weighted residuals, or the Galerkin, method is applied in which the governing equations are satisfied in an integral mean sense (Zienkiewicz and Taylor 1989). The details concerning the problem discretization and the time integration method are described below.

### 4.1. Spatial Discretization

The problem is discretized in space by using a mesh of triangular elements. Since in the momentum balance differential equations (16) the spatial derivatives of the velocity components are by one order higher than the spatial derivatives of the pressure, the velocity field is approximated by polynomial functions that are by one order higher than the polynomials approximating the pressure field. The simplest triangular finite elements allowing such approximations are adopted, in which the unknown discrete values of the velocity components are defined in the three triangle vertices, whereas the discrete value of the pressure is defined in one node, located at the triangle barycentre, as depicted in Figure 2. Thus, in each element there are seven discrete quantities to be calculated, six velocity components and one pressure value. Linear variation of the velocity field $\boldsymbol{v}(\boldsymbol{X}, t)$ within the element is assumed, while the fluid pressure $p(\boldsymbol{X}, t)$ is assumed to be constant throughout an element
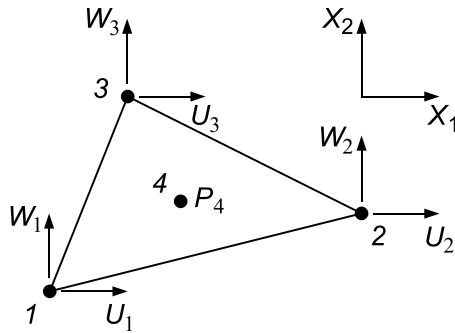
**Fig. 2.** Triangular element with three velocity nodes and one pressure node

area (in consequence, the velocity field is continuous at the element boundaries, whereas the pressure field is discontinuous there). In terms of the nodal parameters $U_j$, $W_j$ ($j = 1, 2, 3$) and $P_4$ (shown in Fig. 2), the velocity and pressure fields within an element are approximated by means of the formulae

$$v_1(X_1, X_2, t) = \Phi_j(X_1, X_2)\, U_j(t)\,,$$

$$v_2(X_1, X_2, t) = \Phi_j(X_1, X_2)\, W_j(t)\,, \quad (j = 1, 2, 3)\,, \tag{21}$$

$$p(X_1, X_2, t) = P_4(t)\,,$$

where $\Phi_j$ ($j = 1, 2, 3$) are linear interpolation (shape) functions, for which standard representations are adopted here, in which simply $\Phi_j = L_j$, with $L_j$ ($j = 1, 2, 3$) being dimensionless triangular area coordinates (Zienkiewicz and Taylor 1989).

By applying the typical finite element routine, the variables $v_1$, $v_2$ and $p$ entering the momentum and mass balance equations, (16) and (17), are replaced by the corresponding expansions (21), and the equations are multiplied by a set of continuous and sufficiently smooth weighting functions. In the Galerkin method, the latter functions are identical to the element interpolation functions, $\Phi_j$ in our case. The resulting relations are then integrated over the whole fluid domain; during this process Green's theorem is used to decrease by one the order of differentiation of the shape functions. As a result, the problem transforms to the solution of a set of algebraic equations which, in matrix notation, is expressed by

$$\boldsymbol{C}\dot{\boldsymbol{u}}(t) + \boldsymbol{K}\boldsymbol{u}(t) = \boldsymbol{f}(t)\,, \quad \boldsymbol{u}(0) = \boldsymbol{u}_0\,. \tag{22}$$

The vector $\boldsymbol{u}$ comprises unknown nodal values of the velocities $U_l$ and $W_l$ and the pressures $P_l$ at all discrete points $l$ of the system. This vector is composed of single element vectors $\boldsymbol{u}^e$, each of them including seven nodal parameters:

$$\boldsymbol{u}^e = (U_1, W_1, U_2, W_2, U_3, W_3, P_4)^T\,. \tag{23}$$

The initial solution vector $\boldsymbol{u}_0$, defining the velocity and pressure fields in the fluid at rest, is assembled from the element vectors $\boldsymbol{u}_0^e$ of the form:

$$\boldsymbol{u}_0^e = \left(0, 0, 0, 0, 0, 0, P_4^0\right)^T, \tag{24}$$

where $P_4^0$ is the initial hydrostatic pressure $p$ at the barycentre of a given element.

The matrices $\boldsymbol{C}$ and $\boldsymbol{K}$ are assembled from respective individual element matrices, $\boldsymbol{c}^e$ and $\boldsymbol{k}^e$ respectively, in a way characteristic of the finite element method. For the adopted elements, with seven degrees of freedom, the matrices $\boldsymbol{c}^e$ and $\boldsymbol{k}^e$ have the dimensions $7 \times 7$ each. The non-zero entries in the element mass matrix $\boldsymbol{c}^e$ are defined by

$$c_{\alpha\beta}^e = \varrho_0 \delta_{ij} \int\limits_A J^{-1} \Phi_r \Phi_s \mathrm{d}A \quad (\alpha, \beta = 1, \ldots, 6), \quad c_{77}^e = -K^{-1} \int\limits_A J \mathrm{d}A, \tag{25}$$

where

$$\alpha = 2(r - 1) + i, \quad \beta = 2(s - 1) + j, \quad r, s = 1, 2, 3; \quad i, j = 1, 2; \tag{26}$$

$\delta_{ij}$ is the Kronecker symbol, and $A$ denotes the plane domain of integration. The non-vanishing components of the element damping matrix $\boldsymbol{k}^e$ are given by

$$k_{\alpha\beta}^e = \int\limits_A \frac{\partial \Phi_r}{\partial X_k} \frac{\partial \Phi_s}{\partial X_m} \left[ \left(\kappa - \tfrac{2}{3}\mu\right) G_{ki} G_{mj} + \mu \left( \delta_{ij} G_{kn} G_{mn} + G_{kj} G_{mi} \right) \right] \mathrm{d}A,$$

$$k_{\alpha 7}^e = - \int\limits_A G_{ki} \frac{\partial \Phi_r}{\partial X_k} \mathrm{d}A, \quad k_{7\beta}^e = - \int\limits_A G_{kj} \frac{\partial \Phi_s}{\partial X_k} \mathrm{d}A \quad (\alpha, \beta = 1, \ldots, 6), \tag{27}$$

with the index relations (26) applying again, and additionally $m = 1, 2$. The non-zero components of the element forcing vector $\boldsymbol{f}^e$, of length 7, are

$$f_\alpha^e = \varrho_0 \int\limits_A J^{-1} b_i \Phi_r \mathrm{d}A \quad (\alpha = 1, \ldots, 6). \tag{28}$$

Since in the above matrix definitions (25) and (27) $c_{\alpha\beta}^e = c_{\beta\alpha}^e$ and $k_{\alpha\beta}^e = k_{\beta\alpha}^e$, and further $k_{\alpha 7}^e = k_{7\beta}^e$, all for $\alpha, \beta = 1, \ldots, 6$, the element matrices $\boldsymbol{c}^e$ and $\boldsymbol{k}^e$ are symmetric, and therefore such are also the global matrices $\boldsymbol{C}$ and $\boldsymbol{K}$.

## 4.2. Time Integration Scheme

Matrix equation (22) expresses a system of first-order differential equations in which the matrices $\boldsymbol{C}$ and $\boldsymbol{K}$ and the loading vector $\boldsymbol{f}$ all depend on current deformation; hence they depend, implicitly, on the unknown solution vector $\boldsymbol{u}$. In order to integrate the equations, a number of standard algorithms, such as the single-step

Newmark and Wilson $\theta$ methods, the multi-step Houbolt method (Bathe 1982), or a family of so-called SSpj methods (Zienkiewicz and Taylor 1991) can be employed (the latter acronym stands for Single-Step with approximation of degree $p$ for equation of order $j$). All these schemes have been developed for dynamic systems described by second-order differential equations. Even though they can be used for solving first-order equations, such as (22), it is more straightforward to use a numerical time-integration method that has been designed specifically for solving first-order equations.

Accordingly, a single-step algorithm, known as the weighted average $\theta$ method (which is different from the above Wilson $\theta$ method) has been applied to solve equation (22). This algorithm is numerically identical to the SS11 method, the simplest member of the SSpj family of methods. Depending on the value of the parameter $\theta$, the adopted method comprises a number of cases: the fully explicit Euler scheme (when $\theta = 0$), the Crank-Nicolson scheme ($\theta = 1/2$), the Galerkin scheme ($\theta = 2/3$), and the fully implicit backward scheme ($\theta = 1$). Application of the $\theta$-method to equation (22) results in the following relation that connects the solution vectors $\boldsymbol{u}_n$ and $\boldsymbol{u}_{n+1}$ on two consecutive time levels, $t_n$ and $t_{n+1}$,

$$(\boldsymbol{C} + \Delta t\,\theta \boldsymbol{K})\,\boldsymbol{u}_{n+1} = [\boldsymbol{C} - \Delta t\,(1 - \theta)\boldsymbol{K}]\,\boldsymbol{u}_n + \Delta t \bar{\boldsymbol{f}}_n \quad (n = 0, 1, 2, \ldots), \qquad (29)$$

where $\Delta t = t_{n+1} - t_n$ denotes the time step length. The vector $\bar{\boldsymbol{f}}_n$ is the time-averaged forcing vector which, assuming its linear variation from $t = t_n$ to $t = t_{n+1}$, is given by

$$\bar{\boldsymbol{f}}_n = (1 - \theta)\boldsymbol{f}_n + \theta \boldsymbol{f}_{n+1}. \qquad (30)$$

Due to the variation of the $\boldsymbol{C}$ and $\boldsymbol{K}$ matrices as we proceed from the old time level $t_n$ to the new level $t_{n+1}$, the solution of (29) does not yield, in general, the vector $\boldsymbol{u}_{n+1}$ which satisfies the motion equation (22) at $t = t_{n+1}$. Hence, (29) gives only some prediction of the solution vector $\boldsymbol{u}_{n+1}$ that needs further correction to satisfy (22) as accurately as possible. Several methods are available to perform the correction, that is to solve the non-linear set of equations represented by (29). The most robust is the Newton-Raphson method which, as long as the initial solution is sufficiently close to the actual solution, ensures quadratic rate of convergence. However, this is achieved at the expense of an additional computational effort required to calculate a new jacobian (or tangent) matrix at each iteration. Here an alternative method is employed in which the correct solution is sought by using the direct (Picard) iteration method. This method converges at a slightly slower rate (Zienkiewicz and Taylor 1991), but in return reduces the computer memory storage and the overall computational cost. In the direct method the current approximation to the solution vector $\boldsymbol{u}_{n+1}^i$ in (29) is immediately used to modify the matrices $\boldsymbol{C}$ and $\boldsymbol{K}$ and the loading vector $\bar{\boldsymbol{f}}$ (dependent on current deformation) before proceeding to the next iteration $i + 1$ ($i = 0, 1, 2, \ldots$). By writing equation (29) in a form

$$\boldsymbol{A}_n \boldsymbol{w}_{n+1} = \boldsymbol{q}_n, \qquad (31)$$

where $q_n$ can be viewed as an effective loading vector acting during the $n$-th time-step, the Picard method is described by the recurrence formula

$$A_{n+1}^i \, w_{n+1}^{i+1} = q_{n+1}^i \quad (i, n = 0, 1, 2, \ldots), \tag{32}$$

where the starting values at the beginning of each time-increment are

$$A_{n+1}^0 = A_n, \quad q_{n+1}^0 = q_n,$$

with analogous relations for $C_{n+1}^0$, $K_{n+1}^0$ and $f_{n+1}^0$. $C_0$, $K_0$, $f_0$ and $w_0$ are the initial values at the start of calculations, at $t = 0$. Having determined from (32) the approximation $w_{n+1}^{i+1}$, a current residual vector $r_{n+1}^{i+1}$ can be evaluated from

$$r_{n+1}^{i+1} = A_{n+1}^{i+1} \, w_{n+1}^{i+1} - q_{n+1}^{i+1}. \tag{33}$$

The iteration process is continued until some convergence condition is satisfied. The latter has been adopted in the form

$$\|r_{n+1}^{i+1}\| \leqslant \varepsilon \, \|q_{n+1}^{i+1}\|, \tag{34}$$

where $\|r\| = (r^T r)^{1/2}$ and $\|q\| = (q^T q)^{1/2}$, and $\varepsilon$ is a tolerance parameter. In the computations the value $\varepsilon = 10^{-7}$ was applied (which is considerably smaller than the value of $10^{-4}$ suggested by (Zienkiewicz and Taylor 1991)), but usually a much better convergence, with the relative error $\|r\| / \|q\|$ of the order $10^{-9}$ to $10^{-10}$, was achieved after four or five iterations.

## 5. Numerical Model and Simulations

### 5.1. FEM Model Description

The general-purpose FEM model constructed for solving two-dimensional problems involving a class of viscous and compressible fluids, as described in the preceding text, has been applied to simulate the phenomenon of transient free-surface wave propagation in water. The numerical model has been implemented on a typical PC with a single 2 GHz processor. One run of the program, for the input data detailed below, required about six to eight hours of computation time.

The following material parameters, pertaining to water, have been adopted in the simulations: the density $\varrho_0 = 10^3$ kg m$^{-3}$, the shear viscosity $\mu = 1.01 \times 10^{-3}$ Ns m$^{-2}$, the bulk viscosity $\kappa = 0$ (signifying the Stokes liquid), and the compressibility modulus $K = 2.04 \times 10^9$ Pa.

The flow problem has been solved in a domain of a simple geometry, sketched in Fig. 3, in which the liquid at rest occupies a rectangle of height $H$ and length $L$. The wall $AB$ can move to generate the water flow, and the walls $CD$ and $AD$ are fixed. Hence, the water horizontal velocity has been prescribed on the wall $AB$ as a function of time, while the horizontal velocity on the wall $CD$ and the vertical
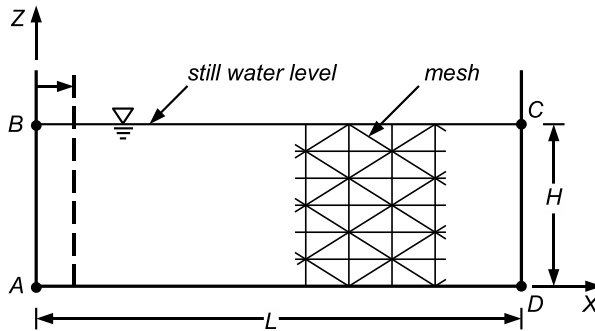
**Fig. 3.** Initial fluid domain geometry for a flow over the horizontal bottom

velocity on the wall $AD$ are zero. The dimensions of the flow domain have been assumed as those corresponding to a laboratory flume. Hence, $H = 60$ cm and $L = 15$ m have been adopted. The latter length parameter has been set to such a relatively small value in order to analyse the problem of wave reflection at a vertical wall $CD$ at $X = L$ occurring at times of the order of a few seconds, rather than tens of seconds, so that the computational effort needed for the time integration of the equations involved can be spared.

The fluid domain has been covered by a regular mesh of finite elements (see Fig. 3). Several methods of discretization have been explored, with uniform as well non-uniform spacings of nodal points in both, horizontal and vertical, directions, and with different initial dimensions of the elements. The test simulations have shown that, with the number of nodes along the vertical kept constant, making the mesh denser near the free surface does not improve noticeably the accuracy of numerical results. Also increasing the mesh density towards the maker, where the largest changes in the velocity and acceleration fields take place, does not yield any significant effect. Therefore, a mesh with uniform spacings in both the $X$ and $Z$-directions has been used. The results presented below (except a test case discussed in Section 5.2) have been obtained with a mesh consisting of 10 'layers' of elements along the $Z$-axis, and 250 'columns' of elements along the $X$-axis. Hence, the FE mesh consisted of 5000 elements (each of the initial horizontal and vertical sides equal to 6 cm), with the total number of 7761 nodes and 10522 degrees of freedom. This particular mesh, in terms of its $X$-spacing, has been chosen on the basis of numerical experiments conducted for a number of uniform grids. It has turned out that making the grid denser does not practically affect the results; for instance, in the case of 500 elements along the $X$-axis the maximum surface elevations, at chosen times, differ by less than 0.3% from the respective results for 250 elements. On the other hand, with the $X$-spacing decreasing, the accuracy of the results significantly deteriorates. For instance, for the grid with 125 elements in the horizontal direction,

the maximum surface elevations differ by more than 5% compared to the grid with 250 elements.

The time integration was performed by applying a constant-length time step size $\Delta t = 10^{-3}$ s. The latter, assuming that the waves propagate with the velocity $\sim 3$ m s$^{-1}$ (which will be seen in subsequent illustrations), gives, for the undistorted mesh, the value of the Courant number equal to about 0.05. This is a relatively small number, but was required to maintain the numerical stability of the method applied (a comparable magnitude of the Courant number was used by Radovitzky and Ortiz (1998) in their numerical simulations of solitary waves). The time integration was carried out until the time of 10 seconds (usually wave reflection occurred at $t \sim 5$ s), so 10000 time steps in total were required in the simulations, with three or five iterations needed within each time step to attain a convergent solution. The calculations were run with the weighting parameter $\theta$ in (29) of the values ranging from 0.8 to 1.0. Smaller values of $\theta$ (approaching 0.5) resulted, in some cases, in numerical oscillations to appear in the solutions obtained.

## 5.2. Model Validation

In order to validate the numerical model, its predictions have been compared with the results of laboratory experiments conducted by Szmidt and Hedzielski (2007). For comparisons, a set of measurements of the free-surface elevation variation at a distance of 3 m from the wave-maker has been used. In that experiment, the movement of water, of an initial depth of $H = 0.6$ m, was induced by an oscillatory, piston-like translations of a vertical wall, carried out with an angular frequency of 2.90 s$^{-1}$ (equivalent to a period of 2.17 s), generating a surface wave of a length of 4.80 m $= 8H$, propagating with a velocity of 2.22 m s$^{-1}$.

The FE element code was driven by the horizontal velocities calculated from the corresponding displacements measured at the wave-maker wall. A uniform mesh used in these test simulations consisted of 5 'layers' of elements along the vertical and 100 'columns' of elements along the horizontal axis, so that the discrete system had in total 1000 elements, 1606 nodes, and 2212 degrees of freedom. The time integration was performed with the time increment $\Delta t = 10^{-2}$ s, which correspons, for the initial, undistorted mesh, to the Courant number of about 0.15. The numerical predictions and the experimental results are compared in Figure 4. The plot (a) shows the time history of the horizontal displacements of the wave-maker, and the plots in Fig. 4b, illustrate the evolution of the free-surface elevation at the chosen space point (i.e., 3 m from the generator), with the solid line representing the FE results, and the dashed line with the circles showing the experimental data. The plots indicate a good agreement between the theoretical and experimental results. The numerically predicted wave length compares well with that measured in the flume. Some discrepancies between the numerical and actually measured extremal surface elevations can be observed, but these are small — the maximum relative
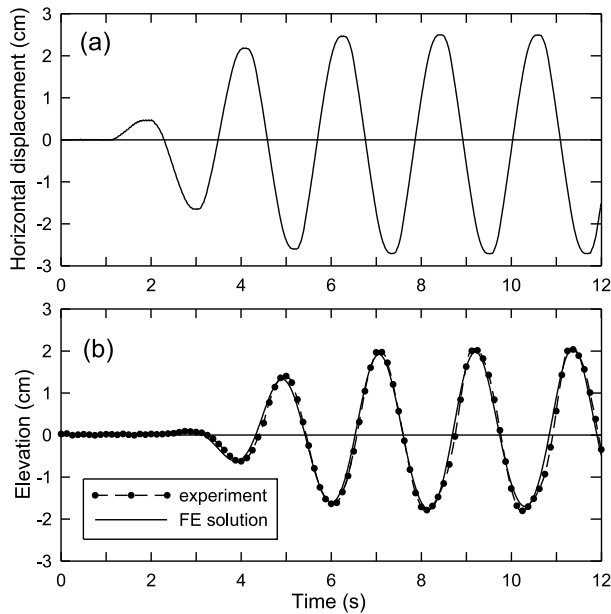
**Fig. 4.** Comparison of the FE model predictions with experimental data: (a) time variation of the wave-maker horizontal displacements, (b) time variation of the free-surface elevation at the distance of 3 m from the wave-maker

differences for the crest elevations are about 2%, and those for the troughs are about 4%. Thus, on the basis of these results, the FE model has been deemed to be constructed properly, before using it in more challenging applications than that represented by the above case of a small-amplitude wave.

The numerical tests have shown that of the two mesh strategies mentioned in Introduction, the second approach, in which the mesh is changed after each time step to trace the changing positions of material particles, has proved to be much more efficient and stable than the first approach, in which the mesh is kept unchanged. Only in the case of very small waves, with the maximum elevations of the order of one centimetre, the two methods can be regarded as comparable. For larger wave heights, and these were by one order of magnitude larger in the cases examined in the simulations described shortly, the method of evolving mesh turned out to be much more advantageous. While in the first, fixed mesh, approach the numerical model typically failed (due to the lack of convergence) within one to two seconds from the start of flow, even with time steps as short as $10^{-4}$ s, the second method maintained its numerical stability throughout the whole period of simulations. For this reason, only the second, convecting mesh method was subsequently used in the simulations.

## 5.3. Illustrations

The objective of the numerical simulations was to predict the behaviour of a strongly non-linear, large-amplitude, transient wave. To generate such a wave, much larger displacements, and displacement-rates, of the wave-maker are required than those actually available in the laboratory flume. For this reason, the model has been run for an assumed motion of the wave generator, rather than using an experimental input. Accordingly, it has been supposed in the simulations that the fluid is set in motion by a piston-type wave-maker vertical wall $AB$ situated at $X = 0$ (Fig. 3), which performs a single translational movement by a distance of $d^*$ before it stops. Hence, the following smooth function, with continuous first and second-order time derivatives at $t = 0$, has been adopted for illustrations to describe the maker horizontal displacement $d_0(t)$:

$$d_0(t) = d^* \left[ 1 - \exp\left(-\tau^3\right) \right], \quad \tau = t/t^*, \tag{35}$$

where $t^*$ is a characteristic time scale. The above relation yields the horizontal velocity $v_0$ and acceleration $a_0$ time-variations expressed by

$$v_0(t) = \frac{d^*}{t^*} \times 3\tau^2 \exp\left(-\tau^3\right),$$
$$a_0(t) = \frac{d^*}{(t^*)^2} \times 3\tau \left(2 - 3\tau^3\right) \exp\left(-\tau^3\right). \tag{36}$$

The above three functions, in their dimensionless forms $d_0/d^*$, $v_0 \, t^*/d^*$ and $a_0 \, (t^*)^2/d^*$, plotted against the normalized time $\tau$, are depicted in Fig. 5.
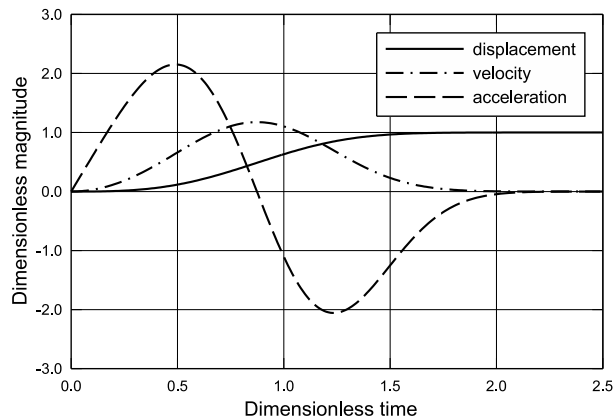


**Fig. 5.** Assumed time variations of the normalized horizontal displacement, velocity and acceleration generated by the wave-maker

Figure 6 illustrates the evolution of the free-surface elevation of a wave induced by moving the maker wall by a distance of $d^* = 20$ cm, with the value of the
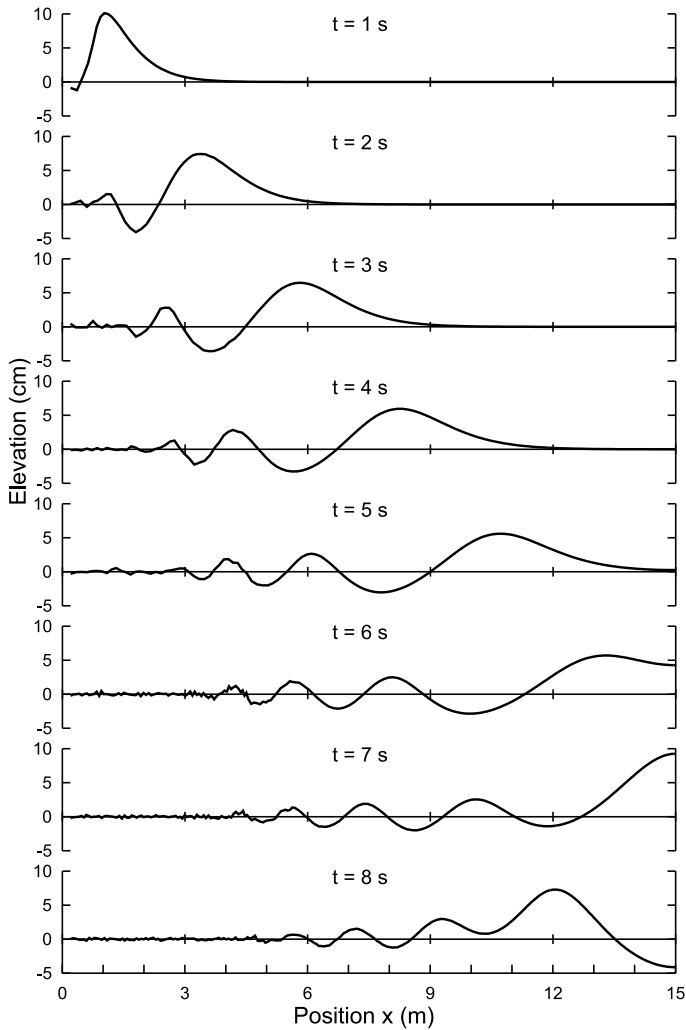
**Fig. 6.** Evolution of the free-surface elevation along the flume length, for the total wave-maker horizontal displacement $d^* = 20$ cm and the characteristic time $t^* = 0.5$ s

characteristic time $t^* = 0.5$ s. For such a movement, the maximum horizontal fluid velocity at the maker surface is equal to $\sim 47$ cm/s, and is generated at a time of $\sim 0.44$ s. The resulting wave has the maximum elevation, reached at $t = 0.5$ s at the maker wall, equal to about 13.7 cm. The plots in the figure demonstrate a characteristic pattern: a smooth shape of the front of the wave, followed by a train of smaller-magnitude troughs and crests, with the surface elevation becoming more and more irregular with an increase of the distance from the wave maker. This clearly indicates the dispersive character of the wave generated, with smaller, and hence slower, waves lagging behind the leading wave. Apart from the above physical reasons, the irregularities of the free surface elevations near the moving wall can

be obviously attributed, to some extent, to an insufficient spatial resolution of the mesh, which is unable to capture the waves of the lengths of the order of a single finite element size.

As can be seen in Figure 6, the reflection of the wave at the vertical wall $X = L = 15$ m starts at a time of about 5 s. After that time, with the reflected leading wave getting larger, an interaction between the waves travelling in opposite directions occurs, giving rise to more variable free-surface profiles in the region adjacent to the wall $Z = L$. These profiles, however, still retain their smooth shape until the time when the leading reflected wave meets with the train of short and irregular waves incoming from the wave-maker direction.

Corresponding to the latter figure are the plots in Figure 7, showing the time variation of the free-surface profile, for $t \leq 5$ s, and enabling better comparisons of the relative changes in the wave magnitude with increasing time.
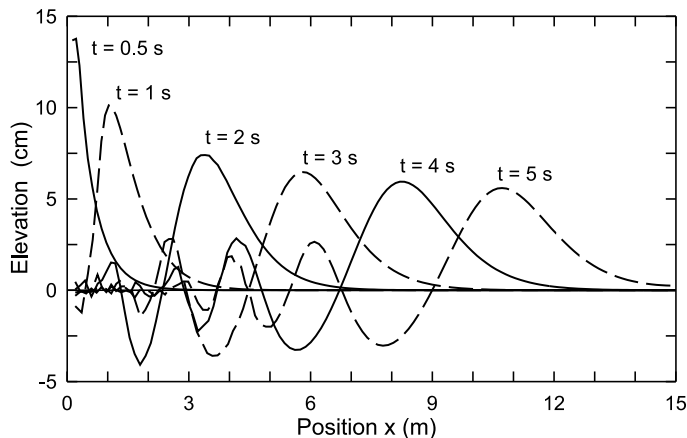


**Fig. 7.** Evolution of the free-surface elevation along the flume length for $t \leq 5$ s, for the total wave-maker horizontal displacement $d^* = 20$ cm and the characteristic time $t^* = 0.5$ s.

In the subsequent diagrams, still for the wave excitation defined by the parameters $d^* = 20$ cm and $t^* = 0.5$ s, the plots illustrating the variations of free-surface displacements with time at a chosen set of locations are presented, corresponding to the form of results that are usually recorded at laboratory measurements. Hence, for a set of the positions $X/L = 0$, 0.2, 0.4 and 0.6, corresponding to $X = 0$, 3 m, 6 m and 9 m, respectively, the time variations of the surface elevations are shown in Figure 8. Similarly, in the following Figure 9, the time changes in the horizontal free-surface displacements at the same set of $X$-locations as above are displayed. One can note in this figure that the model-predicted horizontal movements of the free surface can be nearly as large as 30 cm, that is equal to nearly half of the water depth. Again, the same features as in Figures 6 and 7 can be observed, that is the
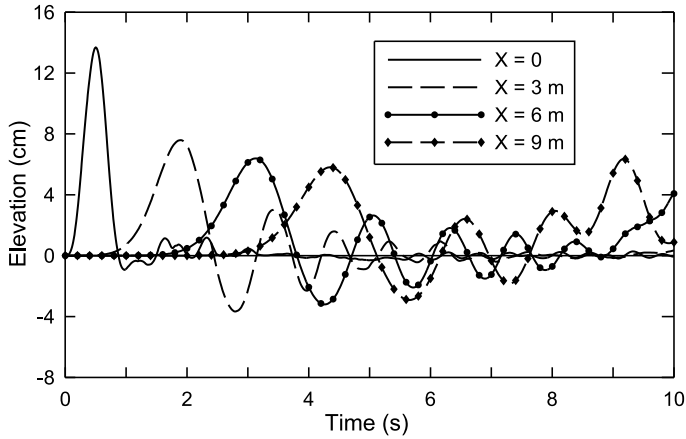
**Fig. 8.** Evolution of the free-surface elevations at chosen locations $X$, for the total wave-maker horizontal displacement $d^* = 20$ cm and the characteristic time $t^* = 0.5$ s
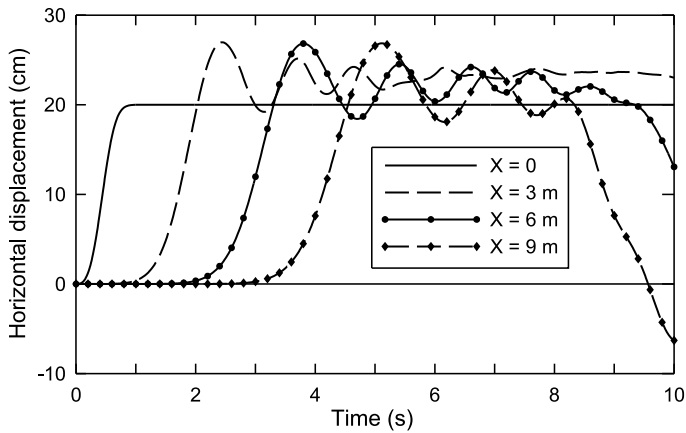


**Fig. 9.** Evolution of the free-surface horizontal displacements at chosen locations $X$, for the total wave-maker horizontal displacement $d^* = 20$ cm and the characteristic time $t^* = 0.5$ s

smooth variations in the free-surface displacements in the leading part of the wave, and more irregular variations in the trailing part of the wave.

Finally, in Figures 10 and 11 the evolution of the free-surface elevation along the flume length is shown for different, than previously considered, combinations of the $d^*$ and $t^*$ parameters. Figure 10 illustrates the case in which the wave-maker wall $AB$ moves in the negative $X$-direction, that is away from the water domain, within the same time period as used in preceding simulations. Hence, the model parameters have been set to $d^* = -20$ cm and $t^* = 0.5$ s. The comparison of the plotted surface profiles with those displayed in Fig. 6 demonstrates that, due to the strong geometric non-linearity of the phenomenon, the two cases yield surface profiles which are not, even approximately, mirror images with respect to the still
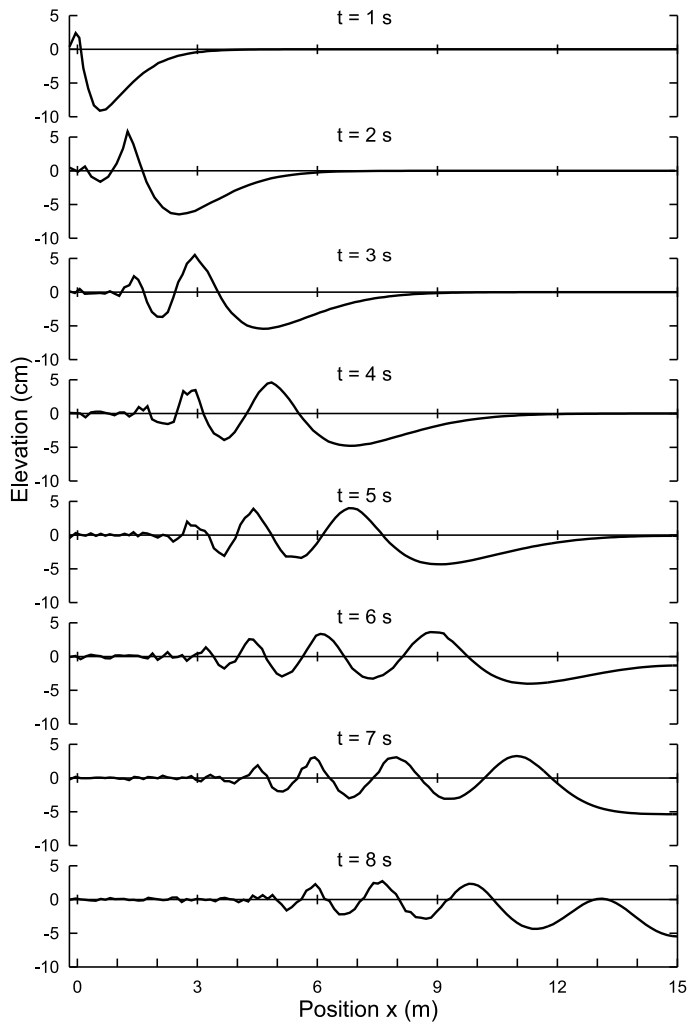
**Fig. 10.** Evolution of the free-surface elevation along the flume length, for the total wave-maker horizontal displacement $d^* = -20$ cm and the characteristic time $t^* = 0.5$ s

water line. The two sets of plots also show that the case of the wall moving away from the water is more difficult to treat numerically. The indication of this feature are the numerical oscillations that are now more numerous and pronounced (especially for the times values of 6, 7 and 8 s) than those in the case illustrated in Fig. 6 — even though the time step length used to obtain the results in Fig. 10 was reduced to $\Delta t = 5 \times 10^{-4}$ s, which is half of the value used in the other examples.

Figure 11 shows the time variation of the free-surface elevation for the case of the wave excitation time being twice as long as that illustrated in Figure 6, that is for $t^* = 1$ s; the maker horizontal amplitude was again $d^* = 20$ cm. One can note that the overall pattern of the wave propagation, together with its reflection at the
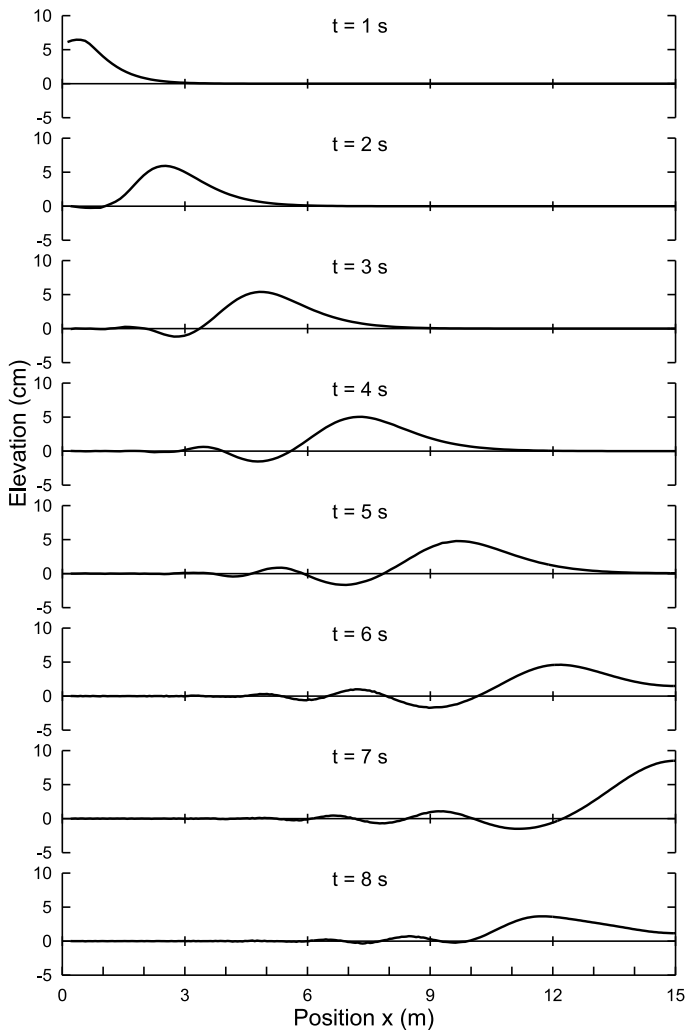
**Fig. 11.** Evolution of the free-surface elevation along the flume length, for the total wave-maker horizontal displacement $d^* = 20$ cm and the characteristic time $t^* = 1.0$ s

rigid wall $CD$, is very similar in both cases. However, due to the slower excitation rate, and in sharp contrast to the case depicted Fig. 10, the surface wave profiles are now much smoother, with practically no numerical instabilities that could be discerned on the free-surface profiles obtained from the simulations.

Besides the cases illustrated in the preceding plots, all obtained for the maker amplitude $d^* = 20$ cm, also the cases of smaller and larger excitation displacements were investigated. The waves generated by the maker wall movement of 10 cm, with the time scale magnitudes $t^*$ of the order of 0.5 s, were all treated successfully. On the other hand, attempts to find stable solutions for the case of $d^* = 30$ cm failed. Simply the waves generated in this case, of the maximum elevation $\sim 20$ cm, that

is about one-third of the still water depth, posed too serious difficulties for the numerical method developed.

## 6. Conclusions

A Lagrangian finite element model for the analysis of Newtonian compressible flows has been constructed. The results of numerical simulations have shown the model robustness in dealing with strongly non-linear problems involving large deformations and moving boundaries, without resorting to complicated algorithms for adaptive mesh refinements. The numerical experiments have demonstrated that the approach based on the progressive reposition of the mesh nodes to follow the movement of material particles is advantageous to the method in which the once generated mesh is kept fixed in space during the computations. The application of the convecting mesh approach enabled the solution of water gravitational wave propagation problems that cannot be satisfactorily solved by using conventional Euler-based approaches. However, the computational cost necessary for obtaining numerically stable and convergent solutions to the problems considered in the work has proved to be substantial. Therefore, the future efforts should concentrate on refining the present model by implementing higher-order finite elements in order to improve the spatial approximation of the variables involved, combined with the application of adaptive time stepping scheme for the temporal integration of the momentum and continuity equations.

## References

Aubry R., Idelsohn S. R. and Oñate E. (2005) Particle finite element method in fluid-mechanics including thermal convection-diffusion, *Comput. Struct.* **83** (17–18), 1459–1475.

Bathe K. J. (1982) *Finite Element Procedures in Engineering Analysis*, Prentice-Hall, Englewood Cliffs, New Jersey.

Braess H. and Wriggers P. (2000) Arbitrary Lagrangian Eulerian finite element analysis of free surface flows, *Comput. Meth. Appl. Mech. Eng.* **190** (1–2), 95–109.

Chadwick P. (1999) *Continuum Mechanics: Concise Theory and Problems*. Dover, Mineola, New York, 2nd edn.

Del Pin F., Idelsohn S., Oñate E. and Aubry R. (2007) The ALE/Lagrangian Particle Finite Element Method: A new approach to computation of free-surface flows and fluid–object interactions, *Comp. Fluids* **36** (1), 27–38.

Feng Y. T. and Perić D. (2000) A time-adaptive space-time finite element method for incompressible Lagrangian flows with free surfaces: computational issues, *Comput. Meth. Appl. Mech. Eng.* **190** (5–7), 499–518.

Idelsohn S. R., Oñate E. and Del Pin F. (2003) A Lagrangian meshless finite element method applied to fluid–structure interaction problems, *Comput. Struct.* **81** (8–11), 655–671.

Idelsohn S. R., Oñate E. and Del Pin F. (2004) The particle finite element method: a powerful tool to solve incompressible flows with free-surfaces and breaking waves, *Int. J. Numer. Meth. Eng.* **61** (7), 964–989.

Idelsohn S. R., Oñate E., Del Pin F. and Calvo N. (2006) Fluid–structure interaction using the particle finite element method, *Comput. Meth. Appl. Mech. Eng.* **195** (17–18), 2100–2123.

Idelsohn S.R., Oñate E. and Sacco C. (1999) Finite element solution of free-surface ship–wave problems, *Int. J. Numer. Meth. Eng.* **45** (5), 503–528.

Liu I.S. (2002) *Continuum Mechanics*, Springer, Berlin.

Löhner R., Sacco C., Oñate E. and Idelsohn S. (2002) A finite point method for compressible flow, *Int. J. Numer. Meth. Eng.* **53** (8), 1765–1779.

Oñate E., Idelsohn S.R., Zienkiewicz O.C. and Taylor R.L. (1996*a*) A finite point method in computational mechanics. Applications to convective transport and fluid flow, *Int. J. Numer. Meth. Eng.* **39** (22), 3839–3866.

Oñate E., Idelsohn S.R., Zienkiewicz O.C., Taylor R.L. and Sacco C. (1996*b*) A stabilized finite point method for analysis of fluid mechanics problems, *Comput. Meth. Appl. Mech. Eng.* **139** (1–4), 315–346.

Ortega E., Oñate E. and Idelsohn S. (2007) An improved finite point method for tridimensional potential flows, *Comput. Mech.* **40** (6), 949–963.

Parrinello F. and Borino G. (2007) Lagrangian finite element modelling of dam–fluid interaction: Accurate absorbing boundary conditions, *Comput. Struct.* **85** (11–14), 932–943.

Rabier S. and Medale M. (2003) Computation of free surface flows with a projection FEM in a moving mesh framework, *Comput. Meth. Appl. Mech. Eng.* **192** (41–42), 4703–4721.

Radovitzky R. and Ortiz M. (1998) Lagrangian finite element analysis of Newtonian viscous flow, *Int. J. Numer. Meth. Eng.* **43** (4), 607–619.

Ramaswamy B. and Kawahara M. (1987) Lagrangian finite element analysis applied to viscous free surface flow, *Int. J. Numer. Meth. Fluids* **7** (9), 953–984.

Souli M. and Zolesio J. P. (2001) Arbitrary Lagrangian-Eulerian and free surface methods in fluid mechanics, *Comput. Meth. Appl. Mech. Eng.* **191** (3–5), 451–466.

Szmidt K. and Hedzielski B. (2007) On the transformation of long gravitational waves in a region of variable water depth: a comparison of theory and experiment, *Arch. Hydro-Eng. Environ. Mech.* **54** (2), 137–158.

Van Brummelen E.H., Raven H.C. and Koren B. (2001) Efficient numerical solution of steady free-surface Navier-Stokes flow, *J. Comput. Phys.* **174** (1), 120–137.

Zienkiewicz O. C. and Taylor R. L. (1989) *The Finite Element Method*, vol. 1, McGraw-Hill, London, 4th edn.

Zienkiewicz O. C. and Taylor R. L. (1991) *The Finite Element Method*, vol. 2, McGraw-Hill, London, 4th edn.